IEEE Access
Multidisciplinary : Rapid Review : Open Access Journal

IEEE POWER & ENERGY SOCIETY SECTION

Received 8 October 2022, accepted 26 November 2022, date of publication 7 December 2022, date of current version 13 December 2022.

Digital Object Identifier 10.1109/ACCESS.2022.3227439

RESEARCH ARTICLE

Multiple-Input Soft-Switching DC–DC Converter to Connect Renewable Energy Sources in a DC Microgrid

ZHUOYA SUN AND SUNGWOO BAE, (Member, IEEE)
Department of Electrical Engineering, Hanyang University, Seoul 04763, South Korea

Corresponding author: Sungwoo Bae (swbae@hanyang.ac.kr)

This work was supported by the Korea Institute of Energy Technology Evaluation and Planning (KETEP) and the Ministry of Trade, Industry & Energy (MOTIE) of the Republic of Korea (No. 20207200000010).

ABSTRACT This paper presents a new multiple-input soft-switching DC–DC Ćuk converter for clean and renewable energy sources. The proposed converter can buck and boost the different voltages of renewable energy sources to produce a constant DC output voltage in a DC microgrid. In the proposed converter, edge-resonant soft-switching modules are used to perform better than the conventional multiple-input Ćuk converter. All switches in the edge-resonant soft-switching modules can realize zero-current switching turn-on and zero-voltage switching turn-off. By using these modules, the proposed converter can achieve lower current stress of the switches, wider soft-switching range, and higher power efficiency than the conventional multiple-input Ćuk converter. These advantages are achieved in the edge-resonant modules, which optimize soft-switching states and costs. In addition, the soft-switching states can be easily achieved because the edge-resonant soft-switching modules have a wide soft-switching range. Furthermore, the proposed converter can independently transfer the generated power from renewable energy sources to the DC microgrid. In this article, the operation principles and performance of the proposed converter are discussed in detail. The theoretical analysis is validated by experimental results obtained from a laboratory-scale prototype and full-scale real-time hardware-in-the-loop experiments.

INDEX TERMS DC–DC power converters, edge-resonant, multiple-input Ćuk converter, zero-current switching, zero-voltage switching.

I. INTRODUCTION

This paper introduces a new multiple-input (MI) soft-switching DC–DC Ćuk converter for renewable energy sources, such as photovoltaic panels, wind turbines, and fuel cells, in a DC microgrid. In the DC microgrid, the increasing installation of renewable energy sources reduces the dependency on fossil-based energy resources. Therefore, it can mitigate environmental degradation. As depicted in Fig. 1, the DC microgrid [1] may include renewable energy systems, such as the photovoltaic (PV) system, wind turbine (WT) system, and fuel cell (FC) system, energy storage system (ESS), and loads. Because these renewable energy sources have different power electronic interfaces [2], each renewable system requires different controllers.

Based on the power–voltage (P–V) curve of PV arrays [3], the maximum power point tracking (MPPT) controllers of the PV system, such as hill climbing and cuckoo search [4], are used to harvest the maximum solar power. In the WT system, the MPPT controllers, such as variable speed control [5], are based on the power-speed curve of WTs [6], [7]. In the FC system, the MPPT controller, such as the perturbation and observation (P&O) [8], is operated by the P–V curve of FCs [9].

After the maximum power of the renewable energy resources is harvested, generated power can be delivered to the DC bus through a multiple-input (MI) converter [10]. The conventional DC microgrid uses a combination of

The associate editor coordinating the review of this manuscript and approving it for publication was S. K. Panda.

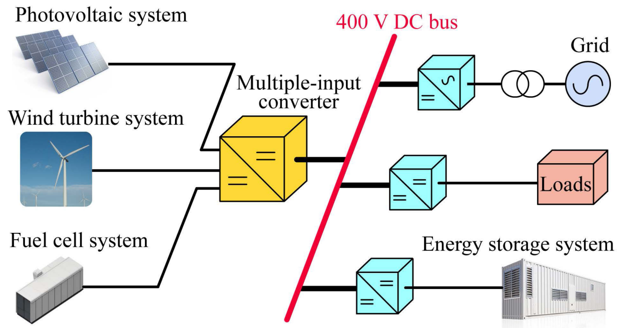

FIGURE 1. The architecture of a multiple-input converter for renewable energy sources in a DC microgrid.

several single-input (SI) converters to deliver power from local renewable energy sources to the main DC bus [11]. However, the disadvantages of the combined SI converters are high costs and relatively complex configurations. To overcome these disadvantages, MI converters have been increasingly implemented in renewable energy systems. Using a single MI converter is more advantageous in compactness, power components, practicability, production costs, and centralized control than using several combined SI converters [10].

The MI converters of previous studies [12], [13], [14], [15], [16], [17], [18], [19], [20] can be categorized into two types: parallel-connected MI converters [12], [13], [14] and time-sharing (TS) MI converters [15], [16], [17], [18], [19], [20]. The parallel-connected MI converters comprise parallel input sources and a single output. All the input sources can deliver power to the output simultaneously or alternately. However, parallel-connected MI converters have complex structures and high costs. On the other hand, TS MI converters, including the MI buck converter [15], MI boost converter [16], MI buck-boost converter [17], MI single-ended primary-inductor converter [18], [19], and MI Ćuk converter [20], have lower cost and complexity than parallel-connected MI converters.

In particular, the MI Ćuk converter has higher structural flexibility among the TS MI converters [21]. In addition, the MI Ćuk converter is a current source converter, wherein the input interface includes an inductor for reducing the input current ripple [22]. Hence, the input current ripple from input sources, such as FCs and PV modules, can be reduced using this converter. Although the MI Ćuk converter is adopted in various applications, such as the wind and PV hybrid power systems [23], [24], its drawbacks of low power efficiency and high current stress of the switches remain.

In order to overcome the aforementioned shortcomings of the conventional MI Ćuk converter, this paper presents a new MI soft-switching Ćuk converter. The proposed converter employs edge-resonant soft-switching modules to realize soft-switching topologies and exhibit improved performance compared to the conventional MI Ćuk converter. In the proposed converter, the turn-on and turn-off states of all the switches can achieve zero-current switching (ZCS) and zero-voltage switching (ZVS), respectively. Thus, the switching loss of all the switches is reduced, and the overall efficiency of the proposed converter is enhanced. In addition, the current stress of the switches is an essential element that affects the cost of implementation and parasitic components of switches. The proposed converter significantly reduces the current stress of switches compared to the conventional MI Ćuk converter. Furthermore, the proposed converter has a wide soft-switching range that can easily realize good soft-switching performance at various load conditions. In addition, the proposed converter can operate in the discontinuous conduction mode (DCM) to achieve the soft-switching operation. Moreover, the proposed converter can operate as a conventional MI Ćuk converter under light load conditions.

The contributions of this study are as follows.

1) The proposed converter realizes good soft-switching performance, which facilitates a decrease in switching loss and increases power efficiency.
2) The current stress of switches can be significantly reduced such that low-current-rated switches can be used in the proposed converter.
3) The proposed soft-switching topology has a wide soft-switching range. Thus, the proposed converter can easily achieve soft-switching topologies at various load conditions.

Furthermore, the proposed converter can operate in step-up and step-down. Therefore, the generated power from renewable energy sources can be independently transferred through the proposed converter to the DC microgrid. As various sources have their own voltage and current characteristics, the proposed converter has practical applications.

This paper is organized as follows: Section II introduces the circuit topology and presents an analysis of the operational principles of the proposed MI soft-switching Ćuk converter. The quantified analysis of the proposed converter is discussed in Section III. Section IV presents the experimental results of the proposed converter. Lastly, the conclusions of this study are discussed in Section V.

II. TOPOLOGY AND OPERATION ANALYSIS OF THE PROPOSED CONVERTER

A. TOPOLOGY OF THE PROPOSED CONVERTER

Fig. 2 presents the proposed converter and edge-resonant soft-switching module. As shown in Fig. 2(a), the proposed converter consists of k number of input cells and a common output stage. For the convenience of analysis, it is assumed that, for the input voltage of the input cells, $V_{in\,1} > V_{in\,2} > \ldots > V_{in\,k}$. Fig. 2(b) presents the edge-resonant soft-switching module [25], which includes three diodes (D_1, D_2, and D_3), two active switches (SW_1 and SW_2), a resonant inductor (L_r), and a resonant capacitor (C_r).

The operation principles of the proposed converter are demonstrated by using a two-input case as an example, as shown in Fig. 3. However, the proposed converter topology is not limited to such a two-input case. As shown in Fig. 3, the

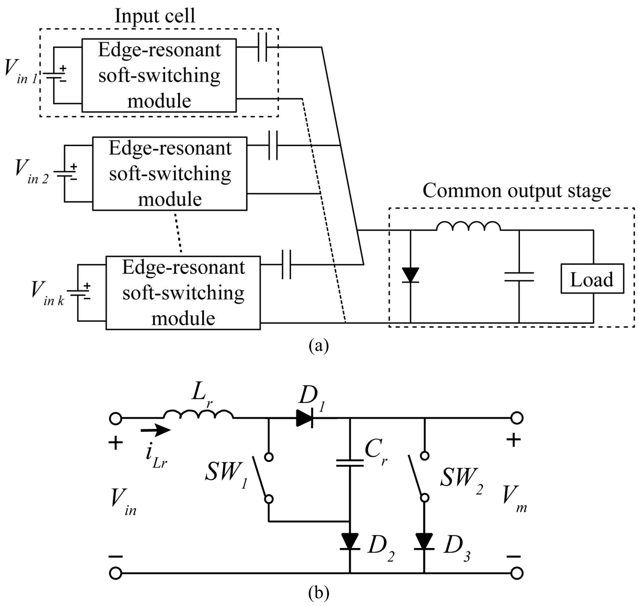

FIGURE 2. Multiple-input soft-switching Ćuk converter. (a) Circuit schematic of the proposed converter. (b) Edge-resonant soft-switching module [25].

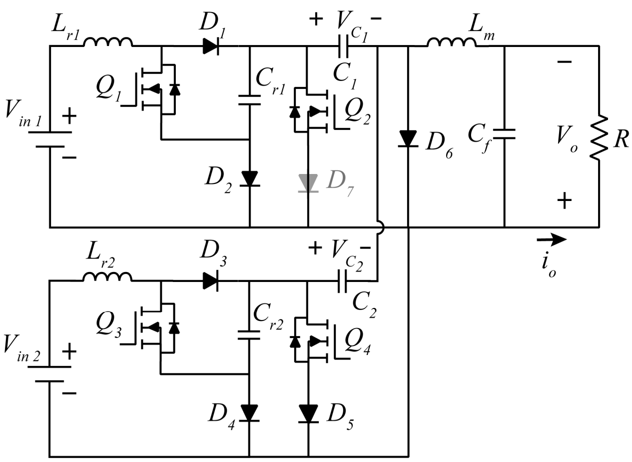

FIGURE 3. Two-input soft-switching Ćuk converter.

proposed converter includes switches (Q_1, Q_2, Q_3, and Q_4), two pairs of resonant components (L_{r1} and C_{r1}, and L_{r2} and C_{r2}), two capacitors (C_1 and C_2), six diodes ($D_1, D_2, \ldots, D_6$), a common output inductor (L_m), a common output capacitor (C_f), and an output load (R). All the switches are assumed to be ideal metal-oxide-semiconductor field-effect transistors (MOSFETs) with body diodes. The proposed converter operates in the DCM with $V_{in\,1} > V_{in\,2}$. In addition, based on the TS theory, a wire can directly connect Q_2 instead of the diode (D_7). However, when more than two input sources are connected to the proposed converter, only the highest voltage of the input source can use a wire instead of the diode (D_7).

B. OPERATION PRINCIPLES ANALYSIS

Fig. 4 and 5 illustrate the equivalent circuit of each operation mode and the theoretical key operational waveforms of the proposed converter, respectively. Fig. 4 illustrates the inductor current flow (i_{Lr1}, i_{Lr2}, and i_{Lm}) for analyzing the proposed converter operation. Moreover, the i_{Lr1} and i_{Lr2} are the input currents of the two input sources $V_{in\,1}$ and $V_{in\,2}$, respectively. As shown in Fig. 5, one switching period (T_s) contains ten operation modes. The gate control signals V_{gs1} and V_{gs2} of the Q_1 and Q_2 have the same duty ratio (d_1), and the gate control signals V_{gs3} and V_{gs4} of the Q_3 and Q_4 have the same duty ratio (d_2).

Mode 1 ($t_0 - t_1$; Fig. 4(a)): At the beginning of this mode, the Q_1, Q_2, Q_3, and Q_4 are turned on with ZCS, because the L_{r1} and L_{r2} are fully discharged before the beginning of this mode. Thus, the increase in current of the four switches can be clamped. The L_{r1} and L_{r2} then start to resonate with the C_{r1} and C_{r2}, respectively. Consequently, the D_1, D_2, D_3, and D_4 are reverse-biased. However, the i_{Lr2} does not flow through the Q_4 and D_5 because $V_{in\,1} > V_{in\,2}$, which results in the D_5 being reverse-biased. The D_6 is also reverse-biased. In this mode, the C_1 delivers power to the L_m and load. The $i_{Lr1}(t)$ and $i_{Lr2}(t)$ can be calculated using

$$i_{Lrk}\,(t) = \left(\frac{V_{ink} + V_{Ck}}{Z_k}\right) \sin\left[\omega_{rk}\,(t - t_0)\right] \quad \text{for } k = 1, 2, \tag{1}$$

where V_{Ck} denotes the average voltage of the C_1 and C_2, $Z_k = \sqrt{L_{rk}/C_{rk}}$, and $\omega_{rk} = 1/\sqrt{L_{rk}C_{rk}}$ for $k = 1, 2$.

Mode 2 ($t_1 - t_2$; Fig. 4(b)): At t_1, the C_{r2} is completely discharged, making the D_3 forward-biased. In this mode, the L_{r2} is linearly charged with the $V_{in\,2}$ through the D_3. Thus, the $i_{Lr2}(t)$ can be expressed as follows:

$$i_{Lr2}\,(t) = \frac{V_{C2} - V_{in\,2}}{L_{r2}}\,(t - t_1) + i_{Lr2}\,(t_1), \tag{2}$$

$$t_1 = t_0 + \frac{1}{\omega_{r2}} \cos^{-1}\left(\frac{V_{in\,2}}{V_{in\,2} + V_{C2}}\right), \tag{3}$$

where $i_{Lr2}(t_1) = \sqrt{V_{C2}\,(2V_{in\,2} + V_{C2})}/Z_2$.

Mode 3 ($t_2 - t_3$; Fig. 4(c)): At t_2, the C_{r1} is fully discharged. The D_1 and D_2 start conducting simultaneously. Therefore, the i_{Lr1} is shared by two branches Q_1–D_2 and D_1–Q_2. During this interval, the $i_{Lr1}(t)$ can be calculated using

$$i_{Lr1}\,(t) = \frac{V_{in1}}{L_{r1}}\,(t - t_2) + i_{Lr1}\,(t_2), \tag{4}$$

$$t_2 = t_0 + \frac{1}{\omega_{r1}} \cos^{-1}\left(\frac{V_{in1}}{V_{in1} + V_{C1}}\right), \tag{5}$$

where $i_{Lr1}(t_2) = \sqrt{V_{C1}\,(2V_{in\,1} + V_{C1})}/Z_1$.

Mode 4 ($t_3 - t_4$; Fig. 4(d)): At t_3, the Q_1 and Q_2 are turned off under ZVS. This is because the C_{r1} is placed in parallel with the Q_1 and Q_2, which can clamp the voltage increase of the Q_1 and Q_2. Consequently, the C_{r1} is charged with the L_{r1} through the D_1 and D_2. During this mode, the $i_{Lr1}(t)$ can be determined by

$$i_{Lr1}\,(t) = I_{Y3} \sin\left[\omega_{r1}\,(t - t_3) + \tan^{-1}\left(\frac{Z_1 i_{Lr1}\,(t_3)}{V_{in1}}\right)\right], \tag{6}$$

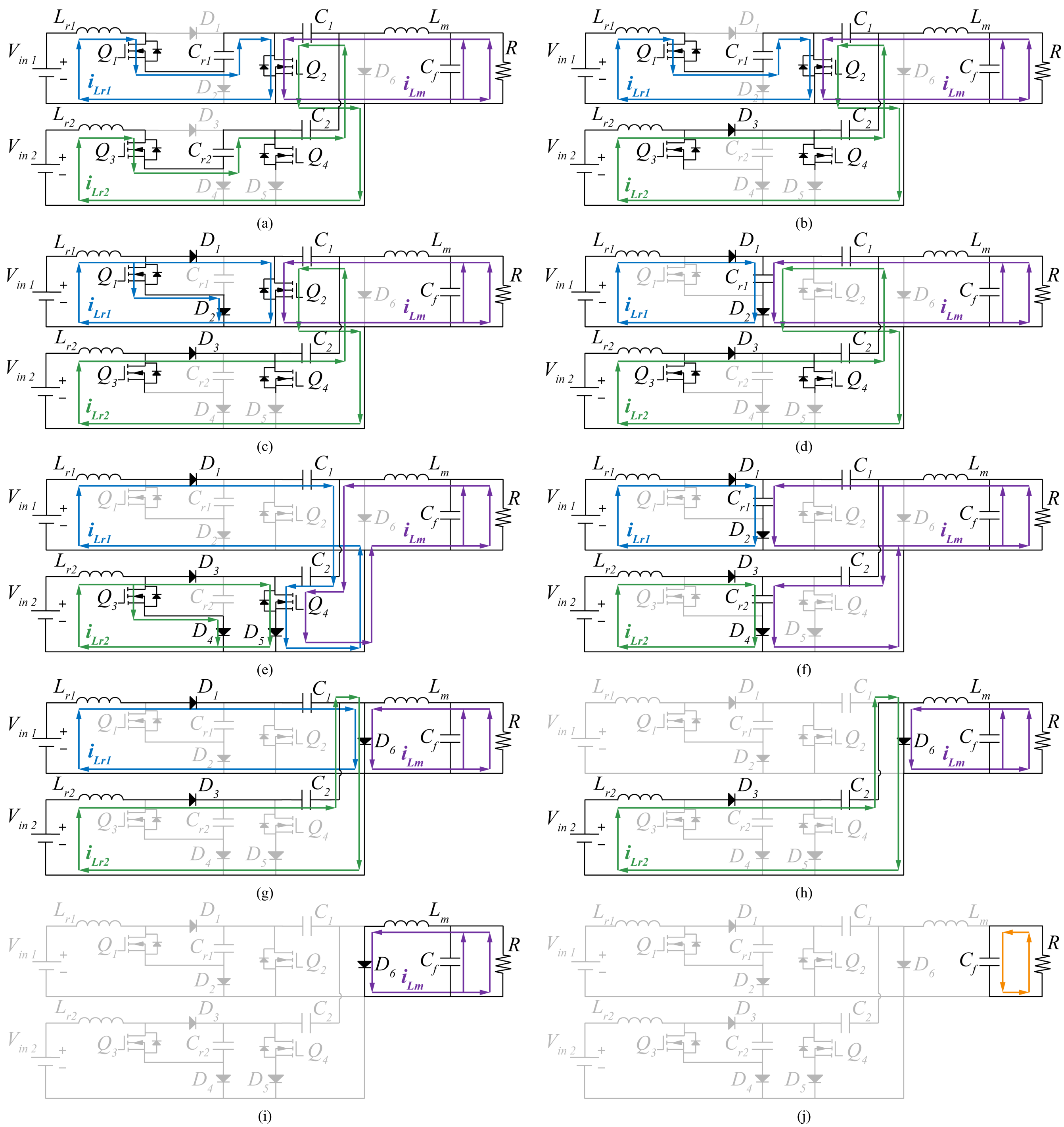

FIGURE 4. Equivalent circuits of the converter for each operation mode. (a) Mode 1, (b) Mode 2, (c) Mode 3, (d) Mode 4, (e) Mode 5, (f) Mode 6, (g) Mode 7, (h) Mode 8, (i) Mode 9, and (j) Mode 10.

where $I_{Y3} = \sqrt{i_{Lr1}^2(t_3) + (V_{in1}/Z_1)^2}$, $t_3 = d_1 T_s$, and $i_{Lr1}(t_3) = (V_{in\,1}/L_{r1})(t_3 - t_2) + i_{Lr1}(t_2)$.

Mode 5 ($t_4 - t_5$; Fig. 4(e)): At t_4, the voltage of C_{r1} increases to a value that equals the summation of $V_{in\,1}$ and the voltage of L_{r1}. Thus, the D_2 is reverse-biased. Meanwhile, the D_4 and D_5 start conducting simultaneously. Subsequently, the i_{Lr2} is shared by two branches $Q_3 - D_4$ and $D_3 - Q_4 - D_5$. In this mode, the C_2 starts to deliver power to the L_m and load instead of the C_1. Accordingly, the $i_{Lr1}(t)$ and $i_{Lr2}(t)$ are calculated as

$$i_{Lr1}(t) = \frac{V_{in1} - V_{C1}}{L_{r1}}(t - t_4) + i_{Lr1}(t_4), \tag{7}$$

$$i_{Lr2}(t) = \frac{V_{in2}}{L_{r2}}(t - t_4) + i_{Lr2}(t_4), \tag{8}$$

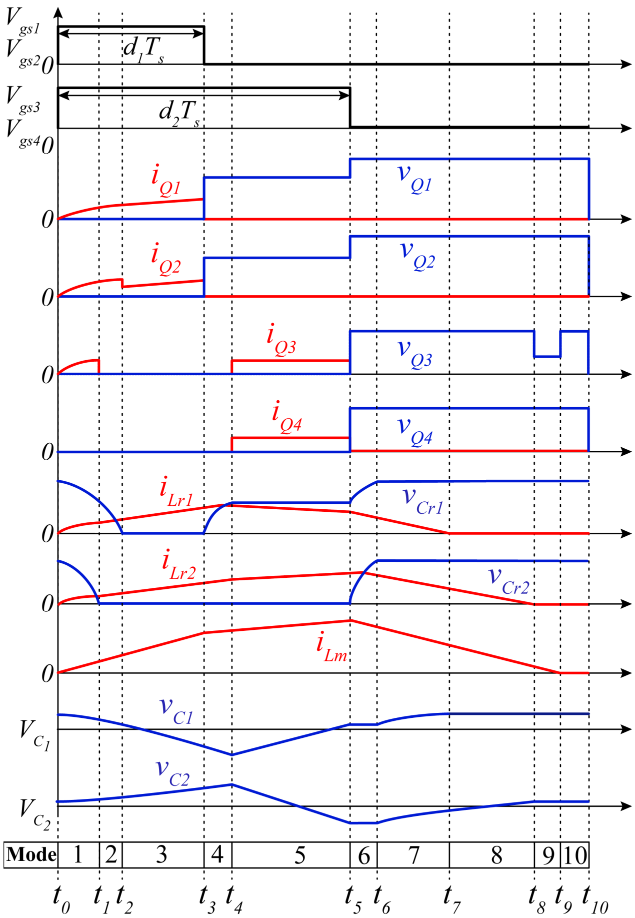

FIGURE 5. Key operational waveforms of the proposed converter.

$$t_4 = t_3 + \frac{1}{\omega_{r1}}\left[\sin^{-1}\left(\frac{V_{in2}}{Z_1 I_{Y3}}\right) + \tan^{-1}\left(\frac{V_{in1}}{Z_1 i_{Lr1}(t_3)}\right)\right], \tag{9}$$

where $i_{Lr1}(t_4) = \sqrt{I_{Y3}^2 - (V_{in\,2}/Z_1)^2}$ and $i_{Lr2}(t_4) = [(V_{C2} - V_{in\,2})/L_{r2}](t_4 - t_1) + i_{Lr2}(t_1)$.

Mode 6 ($t_5 - t_6$; Fig. 4(f)): At t_5, the Q_3 and Q_4 are turned off with ZVS. This is because the C_{r2} is placed in parallel with the Q_3 and Q_4, which can clamp the voltage increase of the Q_3 and Q_4. Then, the C_{r2} is charged with the L_{r2} through the D_3 and D_4. Meanwhile, the D_2 is forward-biased. The C_{r1} continues to charge with the L_{r1}. In this mode, the L_m delivers power to the load instead of the C_2. The $i_{Lr1}(t)$ and $i_{Lr2}(t)$ can be computed using

$$i_{Lr1}(t) = I_{Y5}\sin\left[\omega_{r1}(t - t_5) - \tan^{-1}\left(\frac{Z_1 i_{Lr1}(t_5)}{V_{in2}}\right)\right], \tag{10}$$

$$i_{Lr2}(t) = I_{X4}\sin\left[\omega_{r2}(t - t_5) + \tan^{-1}\left(\frac{Z_2 i_{Lr2}(t_5)}{V_{in2}}\right)\right], \tag{11}$$

where $I_{Y5} = \sqrt{i_{Lr1}^2(t_5) + (V_{in\,2}/Z_1)^2}$, $t_5 = d_2 T_s$, $i_{Lr1}(t_5) = [(V_{in\,1} - V_{C1})/L_{r1}](t_5 - t_4) + i_{Lr1}(t_4)$, $I_{X4} = \sqrt{i_{Lr2}^2(t_5) + (V_{in\,2}/Z_2)^2}$, and $i_{Lr2}(t_5) = (V_{in\,2}/L_{r2})(t_5 - t_4) + i_{Lr2}(t_4)$.

At t_6, the $i_{Lr1}(t_6)$ and $i_{Lr2}(t_6)$ can be expressed as follows:

$$i_{Lr1}(t_6) = \sqrt{I_{Y5}{}^2 - \left(\frac{V_{C1} - V_{in\,1}}{Z_1}\right)^2}, \tag{12}$$

$$i_{Lr2}(t_6) = \sqrt{I_{X4}{}^2 - \left(\frac{V_{C2} - V_{in\,2}}{Z_2}\right)^2}, \tag{13}$$

where $t_6 = t_5 + (1/\omega_{r2})\left[\sin^{-1}((V_{C2} - V_{in2})/(Z_2 I_{X4})) + \tan^{-1}(V_{in2}/(Z_2 i_{Lr2}(t_5)))\right]$.

Mode 7 ($t_6 - t_7$; Fig. 4(g)): At t_6, the C_{r1} and C_{r2} are fully charged and equal the V_{C1} and V_{C2}, respectively, making the D_2 and D_4 reverse-biased. Meanwhile, the D_6 is forward-biased. During this interval, the L_{r1} and L_{r2} discharge to the C_1 and C_2, respectively. This is similar to the functioning of the conventional MI Ćuk converter.

Mode 8 ($t_7 - t_8$; Fig. 4(h)): At t_7, the L_{r1} is completely discharged, making the D_1 reverse-biased. The i_{Lr1} remains zero until the next period starts.

Mode 9 ($t_8 - t_9$; Fig. 4(i)): At t_8, the L_{r2} is completely discharged, making the D_3 reverse-biased. The i_{Lr2} remains zero until the next period starts.

Mode 10 ($t_9 - t_{10}$; Fig. 4(j)): At t_9, the L_m is completely discharged, making the D_6 reverse-biased. The C_f starts to deliver power to the load instead of the L_m. The circuit works in the DCM until the next period starts.

III. QUANTIFIED ANALYSIS OF THE PROPOSED CONVERTER

A. CURRENT STRESS OF SWITCHES

To analyze the current stress of the switches, Q_1, Q_2, Q_3, and Q_4 in the proposed converter are compared with those of the conventional MI Ćuk converter. In the conventional MI Ćuk converter, the switch (S_1) connects to the $V_{in\,1}$, which is the same condition as those of the Q_1 and Q_2. The switch (S_2) connects to the $V_{in\,2}$, which is the same condition as those of the Q_3 and Q_4. In the conventional MI Ćuk converter, the highest current stress of the switches occurs when one input source transfers energy to the output load. Therefore, the conventional MI Ćuk converter exhibits a high peak current, leading to high current stress of the switches. However, in the proposed converter, the current sharing circuits (refer to Fig. 4(c) and (e)) are used to split the input current into two branches during the switch turn-on state. Therefore, the peak current of the switches in the proposed converter is approximately half that of the conventional MI Ćuk converter:

$$I_{Q1(peak)} = I_{Q2(peak)} = 0.5 \times I_{S1(peak)}, \tag{14}$$

$$I_{Q3(peak)} = I_{Q4(peak)} = 0.5 \times I_{S2(peak)}, \tag{15}$$

where $I_{Q1(peak)}$, $I_{Q2(peak)}$, $I_{Q3(peak)}$, and $I_{Q4(peak)}$ represent the peak currents of Q_1, Q_2, Q_3, and Q_4, respectively.

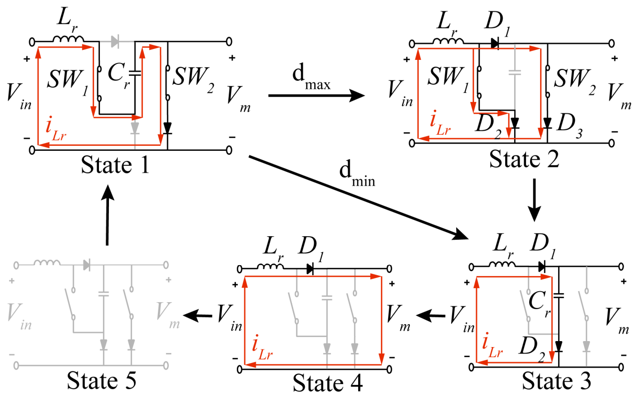

FIGURE 6. Equivalent circuits of the edge-resonant soft-switching module during one switching cycle.

$I_{S1(peak)}$ and $I_{S2(peak)}$ represent the peak currents of S_1 and S_2, respectively.

Therefore, the switches in the proposed converter can select low-current-rated MOSFETs, which is an advantage in terms of reducing the cost of implementation and moderating the effect of parasitic components of switches.

B. SOFT-SWITCHING PERFORMANCE

To determine the soft-switching performance, the operation process of the edge-resonant soft-switching module is used as an analysis example, as shown in Fig. 6. This is because all edge-resonant soft-switching modules have the same operation process. It is assumed that the proposed converter realizes the minimum output power ($P_{o,min}$) at the minimum duty ratio (d_{min}) and the maximum output power ($P_{o,max}$) at the maximum duty ratio (d_{max}). To achieve soft-switching states, the switch turn-on time should be longer than the minimum switching turn-on time.

As shown in Fig. 6, the SW_1 and SW_2 are turned on simultaneously, and the C_r is discharged at State 1. If the proposed converter operates at the d_{min}, the SW_1 and SW_2 are turned off simultaneously once the C_r is completely discharged. Subsequently, the L_r is discharged to zero before the next period starts. However, the current sharing branches (State 2) are not operated during the switch turn-on time. Therefore, the minimum zero-crossing time (t_{min}) of the i_{Lr} (includes States 1, 3, and 4) can be expressed as

$$t_{\min} = \frac{1}{\omega_r}\cos^{-1}\left(\frac{V_{in}}{V_{in}+V_m}\right), \tag{16}$$

where $\omega_r = 1/\sqrt{L_r C_r}$; V_m represents the output of the edge-resonant soft-switching module.

Compared with the d_{min}, the d_{max} includes the current sharing branches (State 2) before the switch turn-off state. Therefore, the soft-switching range is based on the output power range ($P_{o,min} - P_{o,max}$), indicating that the proposed converter has a wide soft-switching range.

C. VOLTAGE CONVERSION RATIO

The voltage conversion ratio is derived based on the power balance between the total input power and output power. To simplify this study, it is assumed that the time origin (t_0) equals zero, and all the components are operating in the ideal solution. Based on the operation analysis, the time integrations of the i_{Lr1} and i_{Lr2} at each sub-mode can be calculated using the expressions listed in Table 1. After summarizing these equations from Table 1, the average input currents ($\overline{i_{Lr1}}$and $\overline{i_{Lr2}}$) can be calculated as follows.

$$\overline{i_{Lr1}} = \frac{1}{T_s}\int_0^{T_s} i_{Lr1}dt = \frac{1}{T_s}\sum\nolimits_{i=1}^{7} Y_i, \tag{17}$$

$$\overline{i_{Lr2}} = \frac{1}{T_s}\int_0^{T_s} i_{Lr2}dt = \frac{1}{T_s}\sum\nolimits_{j=1}^{6} X_j. \tag{18}$$

The relationship between the output load (R) and two input power sources ($V_{in\,1}$ and $V_{in\,2}$) of the proposed converter can be expressed as

$$V_{in\,1}\overline{i_{Lr1}} + V_{in\,2}\overline{i_{Lr2}} = \frac{V_o^2}{R}, \tag{19}$$

where V_o denotes the output voltage of the proposed converter.

Based on (17), (18), and (19), the voltage conversion ratio of the proposed converter at the $P_{o,max}$ is determined as follows:

$$\begin{aligned} &\frac{V_{in\,1}R}{2L_{r1}M_1}\begin{bmatrix} 4C_{r1}L_{r1}V_{C1}M_1 + V_{C1}V_{in\,1}W_1^2 \\ +2L_{r1}W_1 i_{Lr1}(t_2)(V_{in\,1}-M_1) \\ -4L_{r1}W_2 i_{Lr1}(t_4)M_1 + 4C_{r1}^2V_{C1}V_{in\,1} \end{bmatrix} \\ &\quad + \frac{V_{in\,2}R}{2L_{r2}M_2}\begin{bmatrix} 4C_{r2}L_{r2}V_{C2}M_1 + 2(M_2W_3)^2 \\ +V_{C2}V_{in\,2}W_2^2 + 2L_{r2}W_2 i_{Lr2}(t_4) \\ \times(V_{in\,2}-M_2) + 4C_{r2}^2V_{C2}V_{in\,2} \end{bmatrix} \\ &\quad - V_o^2 = 0, \end{aligned} \tag{20}$$

where $M_1 = V_{C1} - V_{in\,1}$, $M_2 = V_{C2} - V_{in\,2}$, $W_1 = d_1T_s - t_2$, $W_2 = d_2T_s - t_4$, and $W_3 = t_4 - t_1$.

In addition, based on the analysis of the soft-switching performance, the voltage conversion ratio of the proposed converter at the $P_{o,min}$ can be determined. If the proposed converter operates at the $P_{o,min}$, modes *3* and *5* (refer to Fig. 4(c) and (e)) will be eliminated among the operation modes. This is because the current sharing circuits are not operated at the $P_{o,min}$ (refer to Fig. 6). Thus, the Y_2, Y_4, X_2, and X_3 are listed in Table 1 equal zero. The $P_{o,min}$ can be calculated as follows.

$$\begin{aligned} P_{o,min} &= V_{in\,1}\overline{i_{Lr1,min}} + V_{in\,2}\overline{i_{Lr2,min}} \\ &= \frac{V_{in\,1}}{T_s}\left(2C_{r1}V_{C1} + \frac{2C_{r1}V_{C1}V_{in\,1}}{V_{C1}-V_{in\,1}}\right) \\ &\quad + \frac{V_{in\,2}}{T_s}\left(2C_{r2}V_{C2} + \frac{2C_{r2}V_{C2}V_{in\,2}}{V_{C2}-V_{in\,2}}\right) \\ &= \frac{2C_{r1}V_{C1}^2V_{in\,1}f_s}{V_{C1}-V_{in\,1}} + \frac{2C_{r2}V_{C2}^2V_{in\,2}f_s}{V_{C2}-V_{in\,2}}, \end{aligned} \tag{21}$$

TABLE 1. Input current expressions in ten operational modes.

Mode	Input Current i_{Lr1}	Input Current i_{Lr2}
1	$Y_1 = \int_0^{t_2} i_{Lr1}\,dt = C_{r1}V_{C1}$	$X_1 = \int_0^{t_1} i_{Lr2}\,dt = C_{r2}V_{C2}$
2		$X_2 = \int_{t_1}^{t_4} i_{Lr2}\,dt = \frac{V_{C2}-V_{in\,2}}{2L_{r2}}(t_4-t_1)^2 - i_{Lr2}(t_1)(t_4-t_1)$
3	$Y_2 = \int_{t_2}^{t_3} i_{Lr1}\,dt = \frac{V_{in\,1}}{2L_{r1}}(d_1T_s-t_2)^2 - i_{Lr1}(t_2)(d_1T_s-t_2)$	
4	$Y_3 = \int_{t_3}^{t_4} i_{Lr1}\,dt = C_{r1}(V_{in\,1}+V_{in\,2})$	
5	$Y_4 = \int_{t_4}^{t_5} i_{Lr1}\,dt = \frac{V_{in\,1}-V_{C1}}{2L_{r1}}(d_2T_s-t_4)^2 - i_{Lr1}(t_4)(d_2T_s-t_4)$	$X_3 = \int_{t_4}^{t_5} i_{Lr2}\,dt = \frac{V_{in\,2}}{2L_{r2}}(d_2T_s-t_4)^2 - i_{Lr2}(t_4)(d_2T_s-t_4)$
6	$Y_5 = \int_{t_5}^{t_6} i_{Lr1}\,dt = C_{r1}(V_{C1}-V_{in\,1}-V_{in\,2})$	$X_4 = \int_{t_5}^{t_6} i_{Lr2}\,dt = C_{r2}V_{C2}$
7	$Y_6 = \int_{t_6}^{t_7} i_{Lr1}\,dt = \frac{L_{r1}i_{Lr1}^2(t_6)}{2(V_{C1}-V_{in\,1})}$	$X_5 = \int_{t_6}^{t_8} i_{Lr2}\,dt = \frac{L_{r2}i_{Lr2}^2(t_6)}{2(V_{C2}-V_{in\,2})}$
8	$Y_7 = 0$	
9		$X_6 = 0$
10		

where $\overline{i_{Lr1,min}}$ and $\overline{i_{Lr2,min}}$ are the average values of i_{Lr1} and i_{Lr2} at $P_{o,min}$, respectively, and f_s is the switching frequency.

Thus, the voltage conversion ratio of the proposed converter at the $P_{o,min}$ is determined as follows:

$$2f_sR\left(\frac{C_{r1}V_{C1}^2V_{in\,1}}{V_{C1}-V_{in\,1}}+\frac{C_{r2}V_{C2}^2V_{in\,2}}{V_{C2}-V_{in\,2}}\right)-V_o^2=0, \tag{22}$$

D. DESIGN CONSIDERATIONS OF THE PROPOSED CONVERTER

This section discusses the design considerations of two pairs of resonant modules $L_{r1}-C_{r1}$ and $L_{r2}-C_{r2}$. The other parameters, such as the C_1, C_2, L_m, and C_f, can be designed to be similar to those of the conventional MI Ćuk converter. Based on the analysis of the soft-switching performance, the design considerations of the resonant modules can be derived based on the $P_{o,min}$ of the proposed converter. Thus, on rearranging (21), the design consideration of C_{r1} and C_{r2} can be expressed as follows:

$$\frac{C_{r1}}{C_{r2}} = \frac{(P_{o,min}V_{C2}-P_{o,min}V_{in\,2}-2C_{r2}V_{C2}^2V_{in\,2}f_s)(V_{C1}-V_{in\,1})}{2C_{r2}(V_{C2}-V_{in\,2})V_{C1}^2V_{in\,1}f_s}. \tag{23}$$

To achieve ZCS at the switch turn-on state, L_{r1} and L_{r2} are required to completely discharge before the beginning of the next period. Thus, $T_s > t_{min}$, which is the discharging time for the L_{r1} and L_{r2}. Hence, based on (16), the L_{r1} and L_{r2} can be calculated as

$$L_{rk} < \frac{1}{C_{rk}\left[f_s\cos^{-1}\left(\frac{V_{in\,k}}{V_{in\,k}+V_{mk}}\right)\right]^2} \quad \text{for } k=1,2. \tag{24}$$

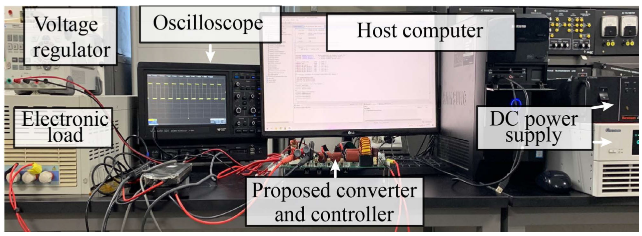

FIGURE 7. Laboratory-scale experimental setup.

Therefore, for the proposed converter designs the L_{r1}, C_{r1}, L_{r2}, and C_{r2}, the aforementioned equations can be used for calculating. Other parameters, such as the C_1, C_2, L_m, and C_f, can be designed with the conventional MI Ćuk converter.

IV. EXPERIMENTAL RESULTS

In this section, the proposed converter was built and tested in the laboratory-scale prototype and full-scale real-time hardware-in-the-loop (HIL) experiments. The laboratory-scale experiment is to verify the operational principles of the proposed converter. The full-scale real-time HIL experiment further analyzes the proposed converter's real-time performance in renewable energy systems.

A. LABORATORY-SCALE EXPERIMENT VERIFICATION

To verify the operational principles, we experimented with a two-input proposed converter that was fabricated with a 100-W laboratory-scale prototype as depicted in Fig. 7. We used two DC power supplies (i.e., Sorensen DCS20-150E and Chroma 62100H-600) for the input power sources of the proposed converter in the laboratory-scale experiment. The prototype converter output was connected to a DC electronic

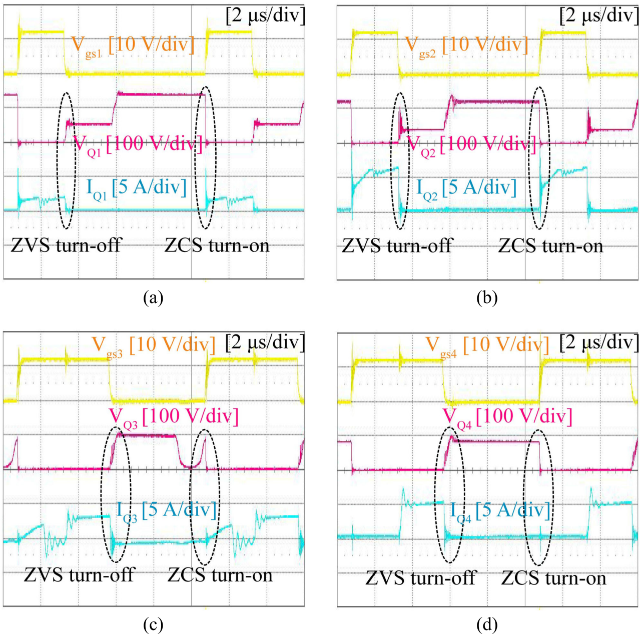

FIGURE 8. Experimental waveforms of the proposed converter switches: (a) Q_1, (b) Q_2, (c) Q_3, and (d) Q_4.

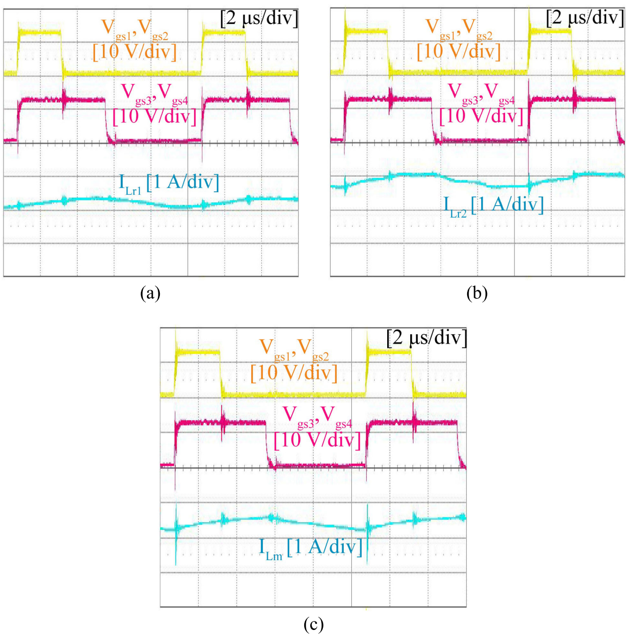

FIGURE 9. Experimental waveforms of the proposed converter inductors. (a) L_{r1}, (b) L_{r2}, and (c) L_m.

load (i.e., Maynuo® M9715B). The prototype converter has two input sources (i.e., 60 V and 12 V) and an output voltage of 48 V as an example for illustrating the switches' and inductors' waveforms in Fig. 8 and 9. Table 2 lists the components of the prototype circuit.

Fig. 8 presents the gate signal, voltage, and current waveforms of the Q_1, Q_2, Q_3, and Q_4, with gate-source voltages of the V_{gs1}, V_{gs2}, V_{gs3}, and V_{gs4}, respectively. As shown in

TABLE 2. Parameters of a laboratory-scale experimental prototype.

Components	Value	Unit
Output power	100	[W]
Input voltage $V_{in\ 1}$ and $V_{in\ 2}$	60 and 12	[V]
Output voltage V_o	48	[V]
Resonant inductor L_{r1}	90	[µH]
Resonant inductor L_{r2}	56	[µH]
Resonant capacitor C_{r1}	12	[nF]
Resonant capacitor C_{r2}	22	[nF]
Capacitors C_1 and C_2	16.4	[µF]
Output inductor L_m	61.2	[µH]
Output capacitor C_f	990	[µF]
Switching frequency f_s	100	[kHz]
MOSFETs	AOT2502L	N/A

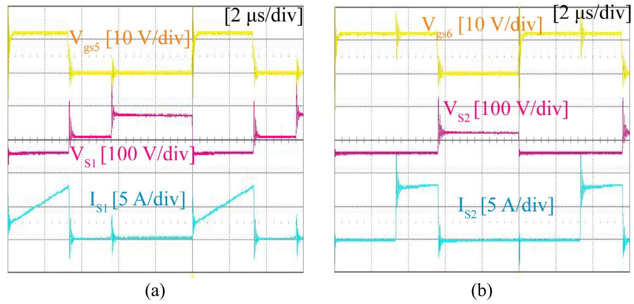

FIGURE 10. Experimental waveforms of the conventional MI Ćuk converter switches. (a) S_1 and (b) S_2.

Fig. 8(a) and (b), the Q_1 and Q_2 are simultaneously turned on with ZCS. This is because the L_{r1} clamps the current increase of the Q_1 and Q_2. During the turn-off process, the C_{r1} clamps the voltage increase of the Q_1 and Q_2 such that the Q_1 and Q_2 are turned off with ZVS. In Fig. 8(c) and (d), the Q_3 and Q_4 are simultaneously turned on with ZCS. This is because the L_{r2} clamps the current increase of the Q_3 and Q_4. However, the i_{Lr2} does not flow through the Q_4 at the initial state. This is because $V_{in\ 1} > V_{in\ 2}$, which causes the D_5 to be reverse-biased. During the turn-off process, the C_{r2} clamps the voltage increase of the Q_3 and Q_4 such that the Q_3 and Q_4 can achieve ZVS. Therefore, the switching loss is significantly reduced because of the soft-switching implementation. Fig. 9 presents the waveforms of the i_{Lr1}, i_{Lr2}, and i_{Lm}. During the turn-off process, the L_{r1} and L_{r2} are completely discharged, which ensures that four switches realize ZCS at the beginning of the next period. The L_m is completely discharged to verify the performance of the proposed converter in the DCM.

To compare the current stress of the switches, the conventional MI Ćuk converter was built, and experiments were performed with the same components and operating conditions. The switch (S_1) in the conventional MI Ćuk converter is connected to the input source (60 V), which is the same condition as those of the Q_1 and Q_2. Meanwhile, the switch (S_2) in the conventional MI Ćuk converter is connected to the input source (12 V), which is the same condition as those of the Q_3 and Q_4. Fig. 10 presents the waveforms of the S_1 and

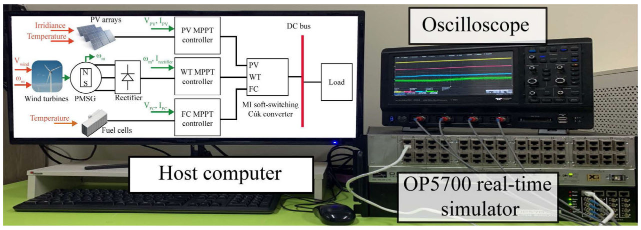

FIGURE 11. Full-scale real-time hardware-in-the-loop experiment setup.

S_2, having gate-source voltages V_{gs5} and V_{gs6}, respectively. On comparing Fig. 8 and 10, the peak current in the S_1 is significantly greater than that in the Q_1 and Q_2. Similarly, the peak current in the S_2 is significantly greater than that in the Q_3 and Q_4. Therefore, the proposed converter can significantly reduce the current stress of switches.

B. FULL-SCALE REAL-TIME HARDWARE-IN-THE-LOOP EXPERIMENT

To analyze the proposed converter's operation in renewable systems, a 100-kW DC microgrid HIL experiment model was built and tested, as depicted in Fig. 11. In this HIL experiment, the DC microgrid model was built in MATLAB/Simulink and complied with the RT-LAB software. Then, the behaviors of the 100-kW DC microgrid operation were verified with the OPAL-RT OP5700 real-time HIL simulator.

1) OPERATION OF THE PROPOSED CONVERTER WITH RENEWABLE ENERGY SOURCES

In this HIL experiment, the proposed converter is connected to three renewable systems, including the PV system, WT system, and FC system. The specifications of these system components are listed in Table 3. In the PV system, PV arrays consist of twenty-eight strings in parallel connection, and each string consists of ten PV modules in series connection. The PV module is modeled with a 200-W AP200 module, as listed in Table 3. Moreover, a boost converter with the global MPPT (GMPPT) control is used in the PV system. Owing to the characteristic of PV arrays, the GMPPT algorithm, which is the cuckoo search with levy flight [4], is adopted to harvest the maximum power of PV arrays in this real-time HIL experiment.

In the WT system, a 24-kW WT system consists of four parallel-connected WT systems, and each WT system is built based on a 6-kW WT [26], a 6-kW permanent magnet synchronous generator (PMSG) [27], a three-phase rectifier, and a buck converter. Moreover, the variable speed control [5] is adopted for harvesting the maximum wind power under different wind speeds.

In the FC system, FCs consist of four parallel-connected FC stacks. The FC stack is modeled with a 5-kW proton-exchange membrane FC H-5000 [28]. Moreover, a boost converter with the MPPT control is used in the FC system. To harvest the maximum power from the FC system, the P&O algorithm [8] is adopted in this HIL experiment.

TABLE 3. Specifications of renewable energy sources connected in the proposed converter in the HIL experiments.

Sources	Components	Value	Unit
PV arrays	Open circuit voltage	333.2	[V]
	Short circuit current	222.3	[A]
	Power at MPP	55.67	[kW]
	Voltage at MPP	263.7	[V]
	Current at MPP	211.1	[A]
PV module	Open circuit voltage	33.3	[V]
	Short circuit current	7.9	[A]
	Power at MPP	198.83	[W]
	Voltage at MPP	26.37	[V]
	Current at MPP	7.54	[A]
WT	Rated power	24	[kW]
	Base wind speed	12	[m/s]
	Air density	1.225	[kg/m^3]
	Blade pitch angle	0	[degree]
PSMG	Rated power	24	[kW]
	Rated speed	153	[rad/s]
	Stator phase resistance	0.425	[Ω]
	Armature inductance	0.395	[mH]
	Magnet flux linkage	0.433	[Wb]
	Number of pole pairs	5	N/A
FCs	Low-voltage shutdown	60	[V]
	Over-current shutdown	360	[A]
	Rated power	20	[kW]
	Nominal voltage	72	[V]
	Nominal current	280	[A]
	Maximum temperature	65	[°C]

Fig. 12(a) illustrates the power of the PV system (P_{PV}), WT system (P_{WT}), FC system (P_{FC}), and the sum of the three systems' power (P_{total}). In this HIL experiment, the irradiance of PV arrays is changed from 1000 w/m^2 to 400 w/m^2 and returned to 1000 w/m^2. The temperature of PV arrays is kept 25 °C. WTs are operated from 12 m/s of wind speed to 4 m/s and returned to 12 m/s, and FCs are operated from 60 liters per minute (L/min) of fuel flow rate to 30 L/min and returned to 60 L/min. Fig. 12(b), (c), and (d) show the voltage and current of the PV arrays (V_{PV}, I_{PV}), WTs (V_{WT}, I_{WT}), and FCs (V_{FC}, I_{FC}), with the correspondent input voltage and current of the proposed converter. It was verified that the proposed converter can operate with different renewable energy systems. Therefore, the proposed converter has practical applications for renewable energy sources.

2) OPERATION OF THE FULL-SCALE PROPOSED CONVERTER

This section presents the HIL experiment results of the full-scale proposed converter with a three-input-source (500 V, 230 V, and 150 V) circuit and a 400-V output voltage as an example for illustrating the switches' waveforms, the power efficiency, and the power loss of the proposed converter, as shown in Fig. 13, 14, and 15. Three renewable energy sources, including the PV, WT, and FC systems, were used as the proposed converter's input sources. The 400-V output voltage was considered as the DC bus voltage. The components of the full-scale proposed converter are listed in Table 4.

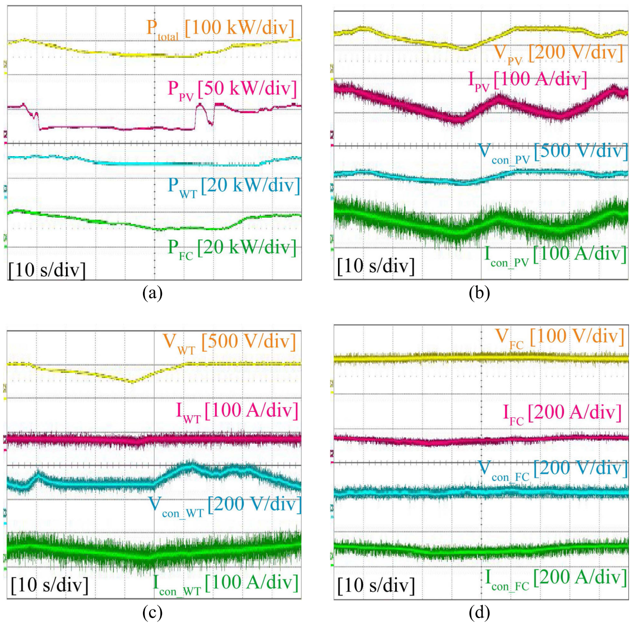

FIGURE 12. HIL experimental waveforms of renewable energy sources. (a) power of renewable energy sources. (b) voltage and current results of the PV system, (c) voltage and current results of the WT system, and (d) voltage and current results of the FC system.

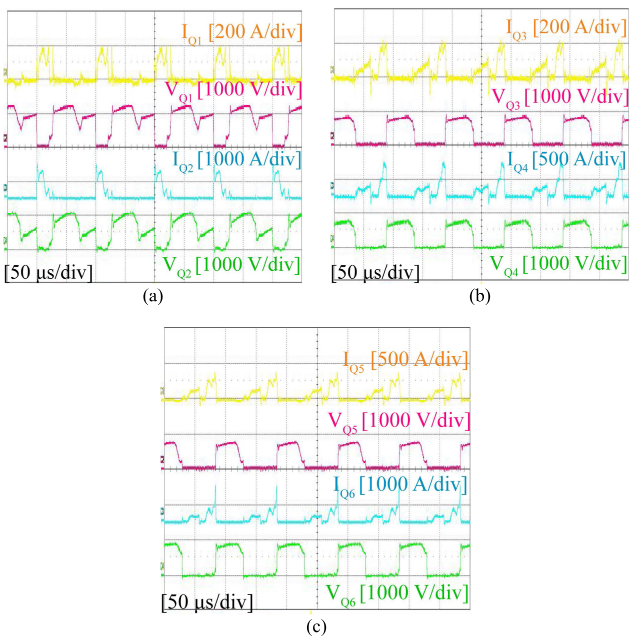

FIGURE 13. Full-scale real-time HIL experimental waveforms of the proposed converter switches: (a) Q_1 and Q_2, (b) Q_3 and Q_4, and (c) Q_5 and Q_6.

Fig. 13 presents the voltage and current waveforms of the Q_1, Q_2, Q_3, Q_4, Q_5, and Q_6. The Q_1 and Q_2 are connected to the 500-V input source. Meanwhile, the Q_3 and Q_4 are connected to the 230-V input source. The Q_5 and Q_6 are connected to the 150-V input source. As shown in Fig. 13, all switches are turned on with ZCS. This is because the resonant inductor (L_{rk}) clamps the current increase of the corresponding switches. During the turn-off process, the resonant capacitor (C_{rk}) clamps the voltage increase of the corresponding switches such that the corresponding switches are turned off with ZVS. Therefore, the switching loss is significantly reduced because of the soft-switching implementation.

TABLE 4. Parameters of the full-scale converter in the real-time HIL experiments.

Components	Value	Unit
Output power	100	[kW]
Input voltage $V_{in\,1}$, $V_{in\,2}$, and $V_{in\,3}$	500, 230, and 150	[V]
Output voltage V_o	400	[V]
Resonant inductor L_{r1}	45	[μH]
Resonant inductor L_{r2}	90	[μH]
Resonant inductor L_{r3}	40	[μH]
Resonant capacitor C_{r1}	1	[nF]
Resonant capacitor C_{r2}	0.1	[nF]
Resonant capacitor C_{r3}	0.2	[nF]
Capacitors C_1, C_2, and C_3	16.4	[μF]
Output inductor L_m	25	[μH]
Output capacitor C_f	10	[mF]
Switching frequency f_s	10	[kHz]
IGBTs	FZ1200R45HL3	N/A

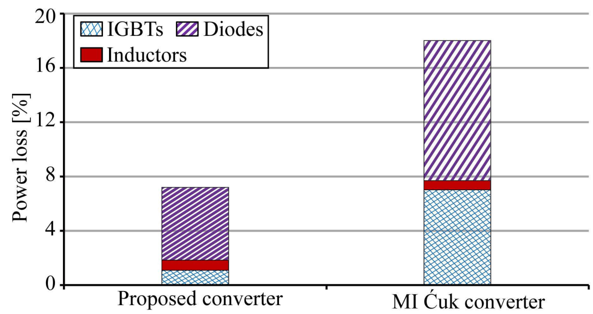

FIGURE 14. Power-loss breakdown comparison of the proposed and the conventional converters at the full-scale real-time HIL experiment.

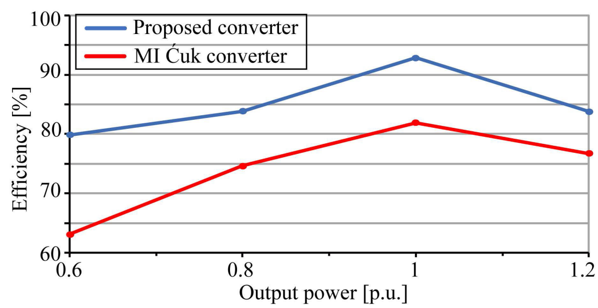

FIGURE 15. Power-efficiency comparison of the proposed and the conventional converters under various output-power conditions in the HIL experiment.

Fig. 14 presents the calculated power loss breakdown when the output power is 100-kW. As shown in Fig. 14, the main power loss in the proposed converter is the diodes loss. Because the proposed converter achieves soft-switching topology, the switching loss is reduced. In addition, to achieve the soft-switching performance, the number of diodes is increased in the proposed converter. Thus, the diodes loss

TABLE 5. Comparative analysis.

Converter	[29]	[30]	[31]	[20]	Proposed converter
Number of input sources	N	N	N	N	N
Number of switches	N+1	N+2	N+1	N	2N
Number of inductors	2	1	N+1	N+1	N+1
Number of capacitors	1	1	2	N+1	2N+1
Number of diodes	N+2	N	2	N+1	3N
Current stress of switches	High	Medium	Medium	Medium	Low
Soft-switching of switches	No	No	Yes	No	Yes
Topology	Boost	buck-Boost	Boost	buck-Boost	buck-Boost
Independent power flow	Yes	Yes	Yes	Yes	Yes
Extension capability	Low	High	High	High	High

comprises a large portion of the power loss in the proposed converter. However, the main power loss in the conventional MI Ćuk converter includes the diodes loss and MOSFETs loss, which is caused by the hard-switching condition. Finally, the total power loss of the proposed converter is less than that of the conventional MI Ćuk converter.

Fig. 15 illustrates the power efficiency of the proposed converter and conventional MI Ćuk converter with the full-scale real-time HIL experiments. As illustrated in Fig. 15, the power efficiency is limitedly promoted under light load conditions. This is because the switching loss has a small portion of the total loss under the light load conditions. However, the switching loss is majorly observed when the output power is increased, thereby improving the power efficiency of the proposed converter. This means that the power efficiency could improve on using soft-switching topologies under heavy-load conditions.

Table 5 presents a comparative analysis of the dual-input hybrid step-up converter [29], the MI converters [30], [31], the conventional MI Ćuk converter [20], and the proposed converter. As shown in Table 5, the current stress of switches in the proposed converter is lower than the MI converter in [20], [29], [30], and [31]. This is because the proposed converter adopts the current sharing circuit to reduce the current stress of each switch. For the soft-switching of switches, the dual-input converter [29], the MI converters [30], and the conventional MI Ćuk converter [20] are incapable of realizing the soft-switching performance. The MI converter [31] only achieves ZVS turn-on. The proposed converter can realize ZCS turn-on and ZVS turn-off. In addition, all converters can independently transfer the power from input sources to the DC microgrid. Moreover, the input sources can be simply extended in [20], [30], and [31], and the proposed converter. Thus, renewable energy sources can easily be connected and transfer the generated energy to the DC microgrid.

V. CONCLUSION

This study proposed a new MI soft-switching Ćuk converter for renewable energy applications. Compared to the conventional MI Ćuk converter, the proposed converter exhibited improved performance by employing edge-resonant soft-switching modules. A detailed analysis of the operational principles and characteristics was performed with a two-input MI soft-switching Ćuk converter. The experimental results confirmed that the proposed converter achieves the soft-switching topology during the switch turn-on and turn-off states. Based on the experimental results, the proposed converter had lower current stress of switches and higher power efficiency than the conventional MI Ćuk converter. Furthermore, the proposed converter had a wide soft-switching range and could operate similarly to the conventional MI Ćuk converter under light-load conditions.

REFERENCES

[1] A. Kwasinski, "Quantitative evaluation of DC microgrids availability: Effects of system architecture and converter topology design choices," *IEEE Trans. Power Electron.*, vol. 26, no. 3, pp. 835–851, Mar. 2011.

[2] Y. Xia, M. Yu, P. Yang, Y. Peng, and W. Wei, "Generation-storage coordination for islanded DC microgrids dominated by PV generators," *IEEE Trans. Energy Convers.*, vol. 34, no. 1, pp. 130–138, Mar. 2019.

[3] R. Bakhshi-Jafarabadi, J. Sadeh, and M. Popov, "Maximum power point tracking injection method for islanding detection of grid-connected photovoltaic systems in microgrid," *IEEE Trans. Power Del.*, vol. 36, no. 1, pp. 168–179, Feb. 2021.

[4] W. Long, S. Cai, J. Jiao, M. Xu, and T. Wu, "A new hybrid algorithm based on grey wolf optimizer and cuckoo search for parameter extraction of solar photovoltaic models," *Energy Convers. Manage.*, vol. 203, Jan. 2020, Art. no. 112243.

[5] S. Bae and A. Kwasinski, "Dynamic modeling and operation strategy for a microgrid with wind and photovoltaic resources," *IEEE Trans. Smart Grid*, vol. 3, no. 4, pp. 1867–1876, Dec. 2012.

[6] Y. Chen, L. Wang, S. Liu, and G. Wang, "A health-oriented control strategy for DC-link capacitor in direct drive wind turbine converter," *IEEE Trans. Power Del.*, vol. 37, no. 5, pp. 4227–4236, Oct. 2022.

[7] X. Wang, D. W. Gao, J. Wang, W. Yan, W. Gao, E. Muljadi, and V. Gevorgian, "Implementations and evaluations of wind turbine inertial controls with FAST and digital real-time simulations," *IEEE Trans. Energy Convers.*, vol. 33, no. 4, pp. 1805–1814, Dec. 2018.

[8] K. Ishaque and Z. Salam, "A review of maximum power point tracking techniques of PV system for uniform insolation and partial shading condition," *Renew. Sustain. Energy Rev.*, vol. 19, pp. 475–488, Mar. 2013.

[9] J. Y. Fam, S. Y. Wong, H. B. M. Basri, M. O. Abdullah, K. B. Lias, and S. Mekhilef, "Predictive maximum power point tracking for proton exchange membrane fuel cell system," *IEEE Access*, vol. 9, pp. 157384–157397, 2021.

[10] A. Affam, Y. M. Buswig, A.-K.-B. H. Othman, N. B. Julai, and O. Qays, "A review of multiple input DC-DC converter topologies linked with hybrid electric vehicles and renewable energy systems," *Renew. Sustain. Energy Rev.*, vol. 135, Jan. 2021, Art. no. 110186.

[11] M. B. Shadmand, R. S. Balog, and H. Abu-Rub, "Model predictive control of PV sources in a smart DC distribution system: Maximum power point tracking and droop control," *IEEE Trans. Energy Convers.*, vol. 29, no. 4, pp. 913–921, Dec. 2014.

[12] S. Hou, J. Chen, T. Sun, and X. Bi, "Multi-input step-up converters based on the switched-diode-capacitor voltage accumulator," *IEEE Trans. Power Electron.*, vol. 31, no. 1, pp. 381–393, Jan. 2016.

[13] F. Akar, Y. Tavlasoglu, E. Ugur, B. Vural, and I. Aksoy, "A bidirectional nonisolated multi-input DC–DC converter for hybrid energy storage systems in electric vehicles," *IEEE Trans. Veh. Technol.*, vol. 65, no. 10, pp. 7944–7955, Oct. 2016.

[14] V. Karthikeyan and R. Gupta, "Multiple-input configuration of isolated bidirectional DC–DC converter for power flow control in combinational battery storage," *IEEE Trans. Ind. Informat.*, vol. 14, no. 1, pp. 2–11, Jan. 2018.

[15] C. M. F. S. Reza, D. D.-C. Lu, and L. Qin, "Single-inductor multiple-source mixer for DC power packet dispatching system," in *Proc. IEEE 2nd Int. Conf. DC Microgrids (ICDCM)*, Jun. 2017, pp. 553–557.

[16] B. Wang, L. Xian, X. Zhang, and H. B. Gooi, "A MPC-based method for single-inductor multiple-input single-output boost converter," in *Proc. IEEE Energy Convers. Congr. Expo. (ECCE)*, Sep. 2018, pp. 4046–4050.

[17] B. G. Dobbs and P. L. Chapman, "A multiple-input DC-DC converter topology," *IEEE Power Electron Lett.*, vol. 1, no. 1, pp. 6–9, Mar. 2003.

[18] S.-Y. Yu, R. Zhao, and A. Kwasinski, "Design considerations of a multiple-input isolated single ended primary inductor converter (SEPIC) for distributed generation sources," in *Proc. IEEE Energy Convers. Congr. Expo.*, Sep. 2011, pp. 3960–3967.

[19] G. Mohanty, "SEPIC based multi input DC-DC converter," in *Proc. IEEE 5th Int. Conf. for Converg. Technol. (I2CT)*, Mar. 2019, pp. 1–4.

[20] S. Bae and A. Kwasinski, "Maximum power point tracker for a multiple-input ćuk DC-DC converter," in *Proc. INTELEC 31st Int. Telecommun. Energy Conf.*, Oct. 2009, pp. 1–5.

[21] Z. Rehman, I. Al-Bahadly, and S. Mukhopadhyay, "Multiinput DC–DC converters in renewable energy applications—An overview," *Renew. Sustain. Energy Rev.*, vol. 41, pp. 521–539, Jan. 2015.

[22] J. Qi and D. D.-C. Lu, "A preventive approach for solving battery imbalance issue by using a bidirectional multiple-input ćuk converter working in DCVM," *IEEE Trans. Ind. Electron.*, vol. 64, no. 10, pp. 7780–7789, Oct. 2017.

[23] S. Bae and A. Kwasinski, "Dynamic modeling and operation strategy for a microgrid with wind and photovoltaic resources," *IEEE Trans. Smart Grid*, vol. 3, no. 4, pp. 1867–1876, May 2012.

[24] N. R. Nair and M. Ebenezer, "Operation and control of grid connected wind—PV hybrid system," in *Proc. Int. Conf. Adv. Green Energy (ICAGE)*, Dec. 2014, pp. 197–203.

[25] Z. Sun and S. Bae, "Multiple-input soft-switching ćuk converter," in *Proc. IEEE Energy Convers. Congr. Expo. (ECCE)*, Oct. 2017, pp. 2272–2276.

[26] M. E. Haque, M. Negnevitsky, and K. M. Muttaqi, "A novel control strategy for a variable-speed wind turbine with a permanent-magnet synchronous generator," *IEEE Trans. Ind. Appl.*, vol. 46, no. 1, pp. 331–339, Jan./Feb. 2010.

[27] W. Cao, N. Xing, Y. Wen, X. Chen, and D. Wang, "New adaptive control strategy for a wind turbine permanent magnet synchronous generator (PMSG)," *Inventions*, vol. 6, no. 1, p. 3, Dec. 2020.

[28] *Horizen H-5000 PEM Fuel Cell Datasheet, Horizon Fuel Cell Technologies*. Accessed: Mar. 7, 2022. [Online]. Available: https://7782216e-8aad-4387-b6a4-b13b0ab6b227.filesusr.com/ugd/047f54_fa621f546cf74b42451427facb47179c.pdf

[29] S. Athikkal, B. Chokkalingam, S. I. Ganesan, B. Lehman, and T. Brunelli Lazzarin, "Performance evaluation of a dual-input hybrid step-up DC–DC converter," *IEEE Trans. Ind. Appl.*, vol. 58, no. 3, pp. 3769–3782, May 2022, doi: 10.1109/TIA.2022.3152973.

[30] L. K. Sahu, H. C. Allamsetty, and S. Ghosh, "Performance analysis of multiple input converter for standalone photovoltaic system," *IET Power Electron.*, vol. 12, no. 5, pp. 1295–1306, May 2019.

[31] R.-J. Wai, C.-Y. Lin, and B.-H. Chen, "High-efficiency DC–DC converter with two input power sources," *IEEE Trans. Power Electron.*, vol. 27, no. 4, pp. 1862–1875, Apr. 2012.

ZHUOYA SUN received the B.S. degree in electrical engineering from the Xinke College, Henan Institute of Science and Technology, Xinxiang, China, in 2012. He is currently pursuing the Ph.D. degree in electrical engineering with Hanyang University, Seoul, South Korea.

SUNGWOO BAE (Member, IEEE) received the B.S. degree in electrical engineering from Hanyang University, Seoul, South Korea, and the M.S.E. and Ph.D. degrees in electrical engineering from the University of Texas at Austin, Austin, TX, USA, in 2006, 2009, and 2011, respectively. From 2012 to 2013, he was a Senior Research Engineer with the Power Center, Samsung Advanced Institute of Technology. From 2013 to 2017, he was with Yeungnam University, Gyeongsan, South Korea. Since 2017, he has been an Associate Professor with the Department of Electrical Engineering, Hanyang University. In 2005, he was awarded the Grand Prize at the National Electrical Engineering Design Contest by the Minister of Commerce, Industry and Energy, Republic of Korea.